EPJ manuscript No.
(will be inserted by the editor)

Study of the cross section determination with the PRISMA spectrometer: the ^{40}Ar+^{208}Pb case

T. Mijatović[1], S. Szilner[1], L. Corradi[2], D. Montanari[3], G. Pollarolo[4], E. Fioretto[2], A. Gadea[5], A. Goasduff[2], D. Jelavić Malenica[1], N. Mărginean[6], G. Montagnoli[3], F. Scarlassara[3], N. Soić[1], A. M. Stefanini[2], C. A. Ur[6], and J. J. Valiente-Dobón[2],

[1] Ruđer Bošković Institute, Zagreb, Croatia
[2] INFN - Laboratori Nazionali di Legnaro, Legnaro, Italy
[3] INFN and Università di Padova, Padova, Italy
[4] INFN and Università di Torino, Torino, Italy
[5] IFIC, CSIC-Universidad de Valencia, Valencia, Spain
[6] Horia Hulubei National Institute of Physics and Nuclear Engineering, Bucharest-Magurele, Romania

Received: date / Revised version: date

Abstract. The PRISMA spectrometer's response function was successfully applied to match three angular and magnetic settings over a wide angular range for measurements of quasi-elastic reactions in ^{40}Ar+^{208}Pb. The absolute scale of cross sections has been obtained by using the Rutherford cross section at the forward angles and the information from the energy distributions measured with the spectrometer without and with coincidences with the CLARA γ-array. The semi-classical model GRAZING has been used to test the unfolding procedure and for comparison with the corrected cross sections.

PACS. 29.30.Aj Magnetic Spectrometers – 25.70.Hi Transfer reactions

1 Introduction

Magnetic spectrometers, with the possibility to completely identify reaction products in nuclear charge, mass and Q-value, always played an important role in the study of transfer reactions (see e.g. Refs. [1, 2] and references therein). A significant improvement in such studies has been achieved in the last decade with the advent of a new generation of large acceptance magnetic spectrometers (PRISMA [3–6], VAMOS [7] and MAGNEX [8]), with solid angles as large as ∼100 msr. Unlike conventional spectrometers where complex magnetic elements are used to focus ions of specific rigidity to a selected position in the focal plane, large solid angle spectrometers are based on simple magnetic elements and complex detection systems, with the identification of the reaction products made through the reconstruction of the ion trajectories.

One of the main observables relating experiment with reaction theory is the absolute value of the cross section, whose knowledge is mandatory to study the importance of the different degrees of freedom acting in the reaction mechanism. In fact one can quantitatively assess the properties of these degrees of freedom only when experimental data are compared with theory incorporating nuclear structure and dynamics informations, which is able to predict absolute cross sections for the different reaction channels [2, 9–13].

In this work we show how one can construct differential cross sections for different angular and magnetic settings over a wide angular range by using the large acceptance spectrometer PRISMA. The adopted procedure is based on the evaluation of the spectrometer's response function, whose reliability has been also tested by a comparison with GRAZING calculations [14–16]. We took as a test case the ^{40}Ar+^{208}Pb system, measured at a beam energy of ∼6.4 MeV/nucleon, near the Coulomb barrier. The kinetic energy of the scattered Ar-like ions ensure good detection resolution while the mass asymmetry of the reaction limits the kinematical broadening thus simplifying our study.

Transfer reactions are usually characterized by a rather wide angular and energy distribution of the reaction products, with cross sections for the different transfer channels spanning several orders of magnitude. Since even in large solid angle spectrometers ions are transmitted within a limited range of angles and momenta, in order to cover the broad distributions of transfer products different spectrometer settings were used. We measured three angular regions, where, for each case, the magnetic fields were adjusted to have the maximal yield of the elastically scattered Ar ions in the center of the focal plane. In each case the transmission of PRISMA was evaluated by using a Monte Carlo simulation of the ion trajectories. This simu-

Send offprint requests to:

lation incorporates the kinematics of the reaction and the geometry of the magnetic elements and detectors. The importance of the precise determination of ion transmission was already demonstrated in other studies [5, 17, 18]. In order to obtain the absolute scale of cross sections, quasi-elastic events were normalized to the Rutherford cross section at the forward angles. Additional information was obtained by employing the PRISMA spectrometer coupled to the CLARA γ-array [4, 19, 20].

2 The PRISMA response function for the ^{40}Ar+^{208}Pb reaction

2.1 The PRISMA spectrometer

In the following we briefly recall the main characteristics of PRISMA relevant for the trajectory reconstruction and the analysis of the response function [4–6]. The PRISMA spectrometer has been designed for the identification of nuclei produced in heavy-ion binary reactions at energies E_{lab}=3-20 MeV/A that are produced with the TANDEM-ALPI-PIAVE accelerator complex of Legnaro National Laboratories. The spectrometer is composed of two ion optical elements, a quadrupole singlet and a dipole magnet, withstanding a maximum rigidity of $B\rho = 1.2$ Tm. Its main characteristics are the large solid angle of $\sim$ 100 msr, which corresponds to an acceptance of $\theta_{lab} = \pm 6°$ in the dispersion (horizontal) plane and $\phi_{lab} = \pm 11°$ in the vertical plane, wide momentum ($\pm 10\%$) acceptance and dispersion of $\Delta p/p \approx 4$ cm/%.

The complete identification of reaction products is achieved via an event-by-event ion trajectory reconstruction [4] using the position, time of flight and energy loss information provided by high resolution entrance and focal plane detectors. The entrance detector is a position sensitive Micro-Channel Plate [21], while the focal plane is an array of Multi-Wire Parallel Plate Avalanche Counters (MWPPAC) [22]. Both of them provide bi-dimensional position information with 1 mm resolution and timing signals for time of flight with sub-nanosecond resolution. The MWPPAC is followed by a multi-parametric transverse field Ionization Chamber (IC) for energy loss and total energy measurements. Since trajectories are different for various products with different p/q ratio, by choosing appropriate magnetic fields it is possible to adjust the system to record a specific range of nuclear products. A schematic layout of PRISMA is depicted in Fig. 1.

The coupling of PRISMA with large γ arrays, CLARA [20] and AGATA demonstrator [23], allowed to perform fragment-γ coincidences, thus studying not only reaction mechanism [4, 19, 24], but also nuclear structure of populated transfer products [25–35]. In this work fragment-γ information employing CLARA was used to derive pure elastic scattering.

2.2 The PRISMA response function

The evaluation of the PRISMA response function is based on a Monte Carlo simulation code that includes the complete description of ion optical elements, magnetic fields and detector geometry. The ion trajectories are calculated on the basis of the detailed knowledge of the magnetic fields. The procedure employs a ray-tracing code, which uses numerical integrators to determine the trajectories of individual rays through the magnetic fields, the latter being calculated by means of the Finite Element Method. This procedure has been successfully employed for the ^{48}Ca+^{64}Ni reaction [5, 19, 36] for one PRISMA angular setting. In this work we applied the same procedure for the ^{40}Ar+^{208}Pb reaction [37–39], but by matching three angular settings.

The reliability of the simulation strongly depends on the detailed knowledge of the magnetic fields and the good matching of the simulated and experimental ones [36]. The first step is, setting the due magnetic fields, to compute the force that acts on the ion moving through the spectrometer. The matching of the experimental and simulated magnetic fields is based on the assumption that, by fixing the ion momentum, each ion charge state will reach the same simulated and experimental focal plane position. In the simulation, the precise setting of the magnetic fields

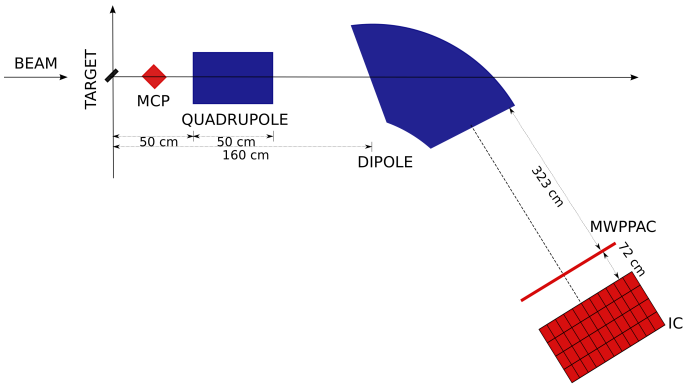

Fig. 1. Schematic layout of the PRISMA spectrometer.

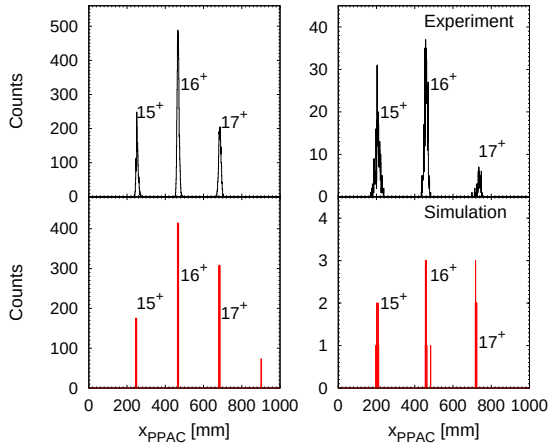

Fig. 2. Comparison of the experimental (top) and simulated (bottom) atomic charge state distributions for ^{40}Ar ions along the optical axis (left) and out of the optical axis (right), as a function of the focal plane position (x_{PPAC}), for PRISMA set at 46°.

proceeds in two steps, one magnetic element at a time. A small number of events with an isotropic distribution are created with a fixed kinetic energy. The ions emerge from the target with different charge states whose probability distribution follows the semi-empirical formula [40]. The same ion with the same kinetic energy is then selected from the data set, so a direct comparison of the two distributions can be made. By comparing the projections of the simulated and experimental distributions around the center of the MCP (the quadrupole field vanishes along the optical axis) one can study the dipole field effects only. After the dipole field is set, the same procedure is applied out of the optical axis to tune the value of the quadrupole field. Adjustments are needed to match the simulated and experimental charge state distributions, mainly due to the approximations made in the reconstruction of the trajectories which are assumed to be planar after the quadrupole and with the magnetic elements considered as ideal [4, 36]. As an example, Fig. 2 shows the experimental and simulated atomic charge state distributions for ^{40}Ar ions along and out of the optical axis. One obtains a quite good agreement, in particular in the focal plane position of the dominant atomic charge states. This procedure is repeated for all measured angular and magnetic settings and at selected kinetic energies, resulting in a similar agreement between the experiment and simulation.

To calculate the response function a simulation of the experimental conditions is needed. The energy losses in the different mylar windows of the MWPPAC and IC detectors are taken into account and the energy loss in the IC is treated in the conventional approximation of the motion of a charged particle in a gas. A 100% intrinsic detection efficiency was assumed over the whole angular range. Two million events of ^{40}Ar ions have been randomly generated with uniform kinetic energy (E_{kin}) distribution and isotropic angular distribution from a point-like source placed at the target position. The E_{kin}, starting from 250 MeV, has been varied down to 100 MeV, corresponding to the lower momentum acceptance limit. Events have been generated with spherical geometry, with an angular range slightly larger than the entrance of the quadrupole. In this way, the generated events completely cover maximal angular and momentum acceptance of PRISMA.

The response function (R) has been defined as the ratio between the transported and input event distributions, and is a function of E_{kin}, θ_{lab} and ϕ_{lab}. The inverse of R, defined as the correction function $f(E_{kin}, \theta_{lab}, \phi_{lab})$, is applied to the transported events. We stress that corrections are made simultaneously on E_{kin} and θ_{lab} (due to azimuthal symmetry the ϕ_{lab} variable can be integrated). Errors induced by the response function can be estimated by building a set of response functions and calculating their average values by using different smoothing procedures [41]. Figure 3 shows transported distributions for different atomic charge states for ^{40}Ar. One sees their non-uniformity, with a shape strongly dependent on the atomic charge state. Figure 4 displays as an example the projections of the correction function on θ_{lab}, for different

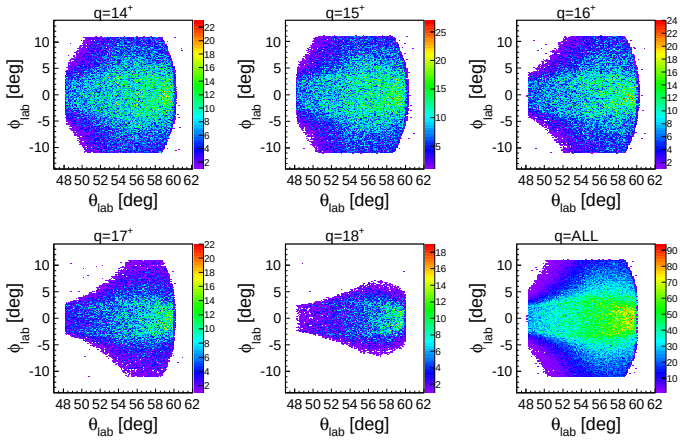

Fig. 3. Transported $\theta_{lab} - \phi_{lab}$ matrices for different atomic charge states for ^{40}Ar integrated over the whole kinetic energy range. θ_{lab} and ϕ_{lab} are the laboratory azimuthal and polar angles, respectively, with respect to the beam axis (the geometrical acceptance is $\theta_{lab} = \pm 6^{\circ}$ and $\phi_{lab} = \pm 11^{\circ}$). Please notice the symmetry in ϕ_{lab}, where $\phi_{lab} = 0^{\circ}$ corresponds to the in plane events.

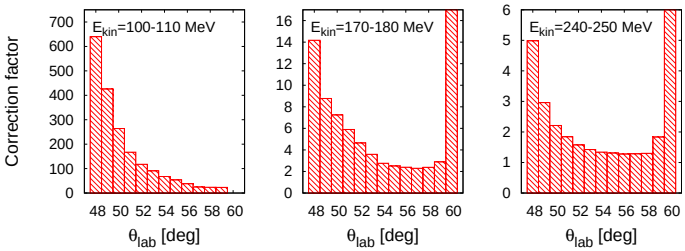

Fig. 4. The correction function projected on θ_{lab} for ^{40}Ar averaged over the labelled kinetic energy intervals.

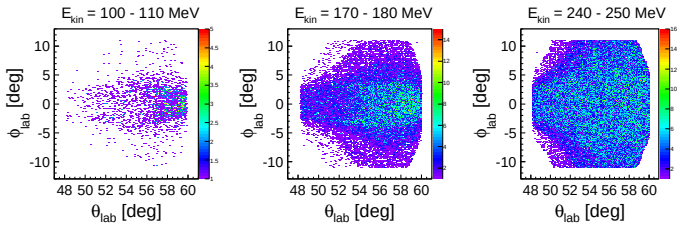

Fig. 5. Transported θ_{lab}-ϕ_{lab} matrices for ^{40}Ar for different (labelled) kinetic energy intervals.

kinetic energy intervals. Figure 5 shows the corresponding transported $\theta_{lab} - \phi_{lab}$ matrices for the same energy ranges. As expected, for all energy intervals the largest corrections are at the borders of the angular acceptance, with large differences in absolute values depending on the kinetic energy of the incoming ion, being the correction factor largest for the lowest energy range. The described procedure has been applied for the different ions detected in the studied reaction.

We tested the correctness of the response function procedure by using the initial energy and angular distributions calculated with the semi-classical model GRAZING [14–16]. The model well reproduces the transfer cross sections in absolute values, as well as the shapes of angular

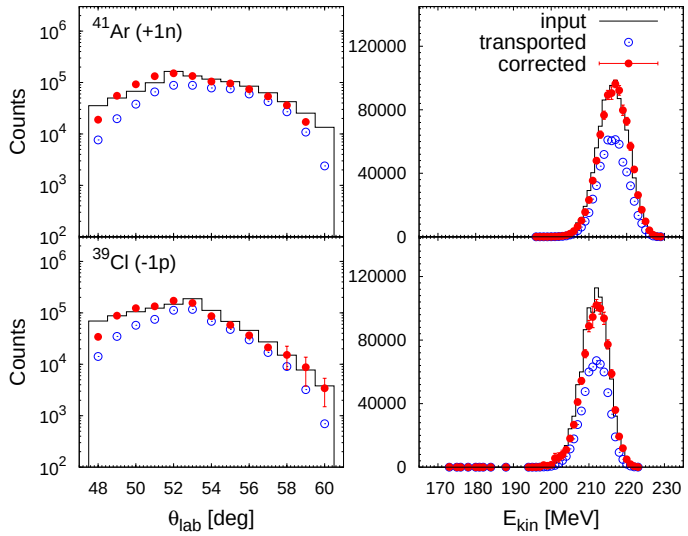

Fig. 6. Angular (left) and kinetic energy (right) distributions for the $(+1n)$ and $(-1p)$ channels. The histograms are the GRAZING input distributions, the blue empty points correspond to the transported distributions at the focal plane and the red full points to the events after the correction function has been applied.

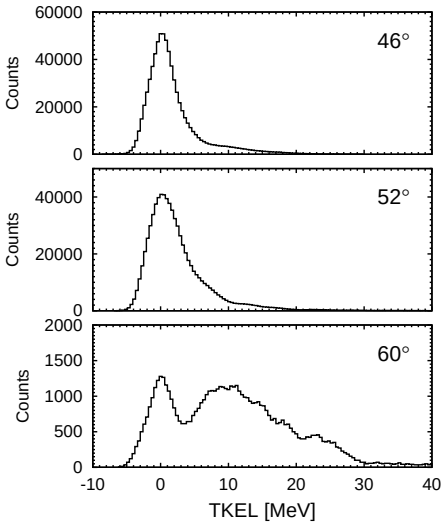

Fig. 7. TKEL spectra for the entrance channel mass partition, with ^{40}Ar detected at the indicated angles, integrated over one $\theta_{\rm lab}$ degree.

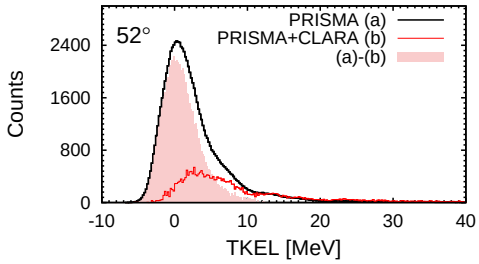

Fig. 8. TKEL spectra for ^{40}Ar integrated over one $\theta_{\rm lab}$ degree. Black full line corresponds to the TKEL spectrum without coincidence with γ rays, while the red one is with additional request of at least one γ ray detected in CLARA. The spectrum without γ coincidences (PRISMA) has been scaled and normalized to the spectrum with γ coincidences (PRISMA+CLARA) in the tail region (above $\sim$ 6 MeV). The red shaded histogram is the spectrum obtained by subtraction.

and total kinetic energy loss distributions [2], in particular the one nucleon transfer channels, $(+1n)$ and $(-1p)$. The GRAZING distributions have been transported through PRISMA and then corrected by using the correction function. The corresponding angular and kinetic energy distributions are displayed in Fig. 6 for the $(+1n)$ and $(-1p)$ channels in the range close to the grazing angle and defined by the spectrometer's acceptance. The excellent agreement between the calculated and corrected event distributions demonstrates the validity of the applied unfolding procedure.

3 Absolute cross sections

3.1 Differential cross section for the entrance channel mass partition

The obtained results give us confidence that we can now apply the unfolding procedure to the measured distributions in order to obtain the cross sections for the different channels. The adopted procedure has been applied to ^{40}Ar+^{208}Pb in the wide angular range obtained by matching the three angular spectrometer's settings and covering an interval of $\sim$20°. For the most forward measured angles the Rutherford cross section has been used for the normalization, thus obtaining the absolute scale in mb/sr for all reaction channels.

We made use of the total kinetic energy loss (TKEL), constructed assuming a binary process and imposing the conservation of momentum. Examples of TKEL spectra for ^{40}Ar detected in PRISMA are shown in Fig. 7 for some selected angles. At more forward angles they are characterized by narrow distributions centered around zero TKEL, representing mainly the elastic components, with tails extending towards larger energy losses. At backward angles the elastic components rapidly drop off and are no more the dominant part of the TKEL. The differential cross sections were extracted by integrating the peak around the zero TKEL (up to the excitation energy of $\sim$ 5 MeV). For completeness, a complementary analysis was carried out by employing fragment-γ coincidences obtained from the coupling of PRISMA to CLARA, which allows us to attribute to each specific reaction product its characteristic γ rays and offers the possibility of separating, at least to some extent, the elastic events. [4,19]. As an example, we plot in Fig. 8 the TKEL spectra for ^{40}Ar at $\theta_{\rm lab}$=52° detected in PRISMA (black full line) and obtained by requiring a coincidence between PRISMA and at least one CLARA γ-ray (red line). The spectra, with and without γ coincidences, are normalized to each other in the tail region, thus obtaining the spectrum by their subtraction (red shaded histogram). One has to keep in

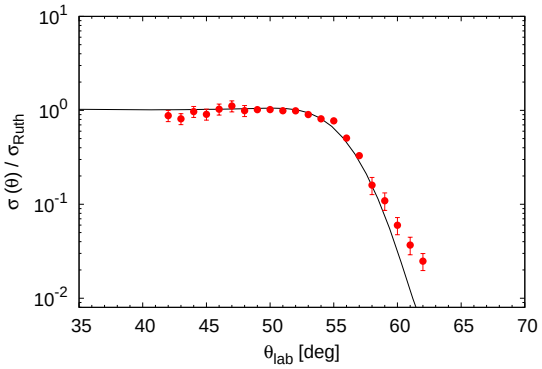

Fig. 9. Experimental (points) and GRAZING (line) calculated differential cross section for the entrance channel mass partition $\sigma(\theta)$ plotted as ratio to the Rutherford cross section $\sigma_{\rm Ruth}$. Shown errors include statistics and systematic errors (up to ∼20%).

mind that this technique depends in a complex way on the energy distribution of the involved γ transitions, their detection efficiency and the multiplicity response of the γ array. The yield of these peaks differ from those previously derived by PRISMA alone by an amount compatible with the uncertainties (up to 20%) including also the subtraction and integration procedures.

The differential cross section derived for each $\theta_{\rm lab}$ in the measured angular range by using PRISMA and corrected by the response function is shown in Fig. 9 as a ratio to the Rutherford cross section (points). One sees the smooth behaviour of the angular distribution, which reflects the correct matching of the three analyzed PRISMA angular settings. In the same Figure, a comparison is made with GRAZING calculations [14–16] (line), which reproduce the experimental data quite well.

3.2 Differential cross sections for the selected transfer channels

The differential cross sections for ^{41}Ar $(+1n)$ and ^{39}Cl $(-1p)$ channels are shown, as selected examples, in Fig. 10. The three different PRISMA angular settings, centered at 46°, 54°, and 59°, allowed to cover most of the total transfer flux. The directly measured distributions are plotted as blue empty circles while the ones corrected for the response function are shown as red full circles. It is important to notice that only after the distributions were corrected for the transmission, smooth differential cross sections were obtained. The comparison between the measured and corrected angular distributions also shows how the spectrometer mostly affects the borders of each PRISMA angular range.

The GRAZING calculations are also plotted in the same Fig. 10 (lines). As already discussed in previously studied cases [2, 42], the theory gives a good prediction of the grazing angle and describes well the forward part of the angular distributions, indicating the quite good geometry and size of the employed potential and the correct treatment of the surface degrees of freedom. At backward

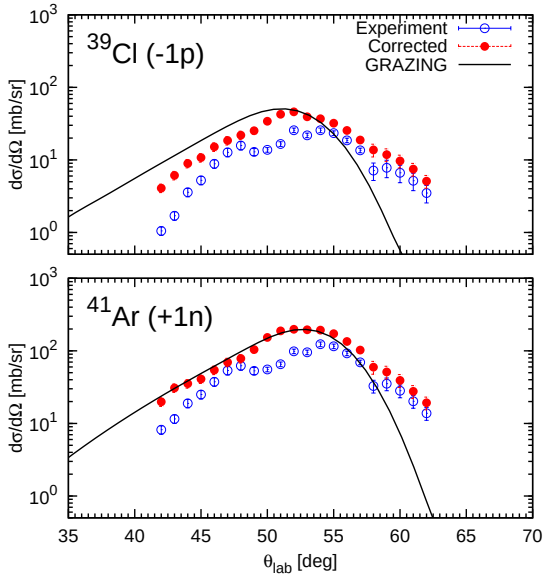

Fig. 10. Experimental angular distributions for $(+1n)$ and $(-1p)$ channels for all three PRISMA settings (46°, 54°, and 59°) joined together. Directly measured distributions are plotted as blue empty circles while the ones corrected for the response function are shown as red full circles. Errors include statistics and systematic errors as in Fig. 9. Black lines are GRAZING calculations.

angles GRAZING displays a sharper fall off of the differential cross sections but we must keep in mind that the behaviour in this region depends on the details of the coupling to the reaction channels. The good obtained agreement, both in shape and magnitude, for the $(+1n)$ and $(-1p)$ channels, is important as they are the main building blocks for computing the more complex channels that are described via a multistep mechanism.

4 Summary

The ^{40}Ar+^{208}Pb reaction was measured with the PRISMA magnetic spectrometer at an energy close to the Coulomb barrier. We measured at three angular and magnetic settings, which were successfully joined, thus spanning an angular range of ∼20° and covering most of the total transfer flux. Accurate simulation of the spectrometer's response function and the extraction of the correction function allowed to obtain these wide angular distributions for the different reaction channels. The reliability of the unfolding procedure was tested with the semi-classical model GRAZING, which well reproduces the transfer cross sections. The response function study was proven to be an essential step in the determination of the absolute differential cross sections.

5 Acknowledgement

The authors are grateful to the LNL Tandem-ALPI staff for the good quality beams and the target laboratory for

the excellent targets. This work was partly supported by the EC FP7 Contract ENSAR (262010). This work has been supported in part by the Croatian Science Foundation under the project 7194. One of the authors (A.G.) has been supported by MINECO, Spain, under the grant FPA2014-57196-C5, Generalitat Valenciana, Spain, under the grant PROMETEOII/2014/019 and EU under the FEDER program.

References

1. K. E. Rehm, Annu. Rev. Nucl. Part. Sci. **41**, 429 (1991).
2. L. Corradi, G. Pollarolo and S. Szilner, J. of Phys. G **36**, 113101 (2009).
3. A. M. Stefanini et al., Nucl. Phys. A **701**, 217 (2002).
4. S. Szilner *et al.*, Phys. Rev. C **76**, 024604 (2007).
5. D. Montanari *et al.*, Eur. Phys. J. A **47**, 4 (2011).
6. L. Corradi *et al.*, Nucl. Instrum. Methods Phys. Res. B **317**, 743 (2013).
7. H. Savajols *et al.*, Nuc. Phys. A **654**, 1027c (1999).
8. A. Cunsolo *et al.*, Nucl. Instrum. Methods Phys. Res. A **481**, 48 (2002).
9. G. R. Satchler, *Direct Nuclear Reactions*, Clarendon Press, Oxford, 1983.
10. R. A. Broglia and A. Winther, *Heavy Ion Reactions*, Addison-Wesley Pub. Co., Redwood City CA, 1991.
11. G. Potel, A. Idini, F. Barranco, E. Vigezzi and R. A. Broglia, Rep. Prog. Phys. **76**, 106301 (2013).
12. L. Corradi *et al.*, Phys. Rev. C **84**, 034603 (2011).
13. D. Montanari *et al.*, Phys. Rev. Lett. **113**, 052501 (2014).
14. A. Winther, Nucl. Phys. A **572**, 191 (1994).
15. A. Winther, Nucl. Phys. A **594**, 203 (1995).
16. personalpages.to.infn.it/∼nanni/grazing/
17. S. Pullanhiotan *et al.*, Nucl. Instrum. Methods Phys. Res. A **593**, 343 (2008).
18. M. Cavallaro *et al.*, Nucl. Instrum. Methods Phys. Res. A **637**, 77 (2011).
19. D. Montanari *et al.*, Phys. Rev. C **84**, 054613 (2011).
20. A. Gadea *et al.*, Eur. Phys. J. A **20**, 193 (2004).
21. G. Montagnoli *et al.*, Nucl. Instrum. Methods Phys. Res. A **547**, 455 (2005).
22. S. Beghini *et al.*, Nucl. Instrum. Methods Phys. Res. A **551**, 364 (2005).
23. A. Gadea *et al.*, Nucl. Instrum. Methods Phys. Res. A **654**, 88 (2011).
24. A. Vogt *et al.*, Phys. Rev. C **92**, 024619 (2015).
25. N. Mărginean *et al.*, Phys. Lett. B **633**, 696 (2006).
26. S. Lunardi *et al.*, Phys. Rev. C **76**, 034303 (2007).
27. J. J. Valiente-Dobón *et al.*, Phys. Rev. C **78**, 024302 (2008).
28. J. J. Valiente-Dobón *et al.*, Phys. Rev. Lett. **102**, 242502 (2009).
29. D. Mengoni *et al.*, Phys. Rev. C **82**, 024308 (2010).
30. D. Montanari *et al.*, Phys. Lett. B **697**, 288 (2011).
31. D. Montanari *et al.*, Phys. Rev. C **85**, 044301 (2012).
32. F. Recchia *et al.*, Phys. Rev. C **85**, 064305 (2012).
33. C. Louchart *et al.*, Phys. Rev. C **87**, 054302 (2013).
34. P. R. John *et al.*, Phys. Rev. C **90**, 021301 (2014).
35. R. Chapman *et al.*, Phys. Rev. C **92**, 044308 (2015).
36. D. Montanari, Ph.D. thesis, *Reaction dynamics of neutron rich nuclei in Ca isotopes with heavy ions and gamma spectroscopy*, University of Milan, 2010 (unpublished).
37. S. Szilner *et al.*, Phys. Rev. C **84**, 014325 (2011).
38. S. Szilner *et al.*, Phys. Rev. C **87**, 054322 (2013).
39. T. Mijatović, Ph.D. thesis, *Study of heavy-ion reactions with large solid angle magnetic spectrometers*, University of Zagreb, 2015 (unpublished).
40. K. Shima *et al.*, Nucl. Instrum. Methods Phys. Res. **200**, 605 (1982).
41. J. S. Simonoff, *Smoothing Methods in Statistics*, Springer, New York, 1996.
42. S. Szilner *et al.*, Phys. Rev. C **71**, 044610 (2005).